

RESEARCH

Open Access



Experimental research on mechanical and impact properties of ceramsite prepared from secondary aluminum dross and municipal solid waste incineration ash

Wangze He^{1,2,3}, Yufei Yang^{1,3}, Xinghan Zhu^{1,3}, Jinzhong Yang^{1,3*}, Yingjie Sun² and Qifei Huang^{1,2,3}

Abstract

With the growth of the industrial aluminum smelting sector, and the increasing proportion of incineration treatment in the field of waste management and disposal, there has been a corresponding increase in the production of secondary aluminum dross (SAD) and municipal solid waste incineration fly ash (MSWIFA) annually. In this research, ceramsite is prepared using SAD, MSWIFA, and municipal solid waste incineration bottom ash (MSWIBA) as raw materials. This study explores the impact of various factors on the mechanical properties of ceramsite and their mechanisms under different conditions, including sintering temperature, raw material ball particle size, raw material silica-alumina ratio, and sintering time. Single-factor experiments demonstrate that the compressive strength of ceramsite initially follows a non-linear ascending trend with increasing sintering temperatures. Additionally, the strength is enhanced with reductions in particle size of the raw material balls, prolongation of the sintering time, and a reduction in the silica-to-alumina ratio of the raw materials. Orthogonal experiments reveal the ideal preparation conditions for ceramsite as follows: a preheating temperature of 400 °C, a preheating duration of 20 min, a sintering temperature of 1270 °C, and a duration of 30 min. Under these conditions, the optimal composition ratio of ceramsite is Si:Al = 3, and the ideal particle size is 0.5 cm. Analysis through X-ray diffraction and scanning electron microscopy revealed the formation of new mineral phases such as sodium feldspar and potassium feldspar in the ceramsite, which display a dense structure under microscopic observation. These contribute positively to the mechanical properties of the ceramsite. Fourier-transform infrared spectroscopy analysis indicates that at a sintering temperature of 1260 °C or when the raw material ball size is 2 cm, the [SiO₄] tetrahedral bands shift to higher wavenumbers, enhancing the degree of polymerization of the glass network in the ceramsite, thereby strengthening its compressive strength. As the silica-alumina ratio of the raw materials decreases and the sintering duration extends, the [SiO₄] tetrahedral bands continue to shift to higher wavenumbers, further enhancing the compressive strength of the ceramsite.

Keywords Ceramsite, Secondary aluminum dross, Mechanical properties, Compressive strength, Hazardous waste material, Municipal solid waste incineration fly ash, Municipal solid waste incineration bottom ash

*Correspondence:

Jinzhong Yang

13366149259@163.com

Full list of author information is available at the end of the article



© The Author(s) 2025. **Open Access** This article is licensed under a Creative Commons Attribution 4.0 International License, which permits use, sharing, adaptation, distribution and reproduction in any medium or format, as long as you give appropriate credit to the original author(s) and the source, provide a link to the Creative Commons licence, and indicate if changes were made. The images or other third party material in this article are included in the article's Creative Commons licence, unless indicated otherwise in a credit line to the material. If material is not included in the article's Creative Commons licence and your intended use is not permitted by statutory regulation or exceeds the permitted use, you will need to obtain permission directly from the copyright holder. To view a copy of this licence, visit <http://creativecommons.org/licenses/by/4.0/>.

1 Introduction

Aluminum dross, a secondary ash byproduct, is produced during the aluminum processing and is classified as a hazardous waste. It is generally divided into primary aluminum dross (PAD) and secondary aluminum dross (SAD). PAD, a non-melting slag, forms on the surface of molten aluminum during the electrolysis process as a result of exposure to air. It is white in color and commonly referred to as white ash. SAD, in contrast, is the residual ash byproduct resulting from the recycling and processing of PAD and waste aluminum materials. It is black in color and is also termed black ash [1]. In recent years, global aluminum production has consistently risen, reaching approximately 68 Mt in 2022, with China accounting for 40 Mt [2] or 59% of the global total. The Primary and secondary aluminum industries generate 3–5 and 10–15% of PAD and SAD, respectively, per ton of molten aluminum produced [3]. This suggests that China's current annual aluminum dross emissions can amount to as much as 6 Mt. PAD is recycled due to its high aluminum content, whereas SAD is typically disposed of through landfilling [4]. However, the release of chemical components (NH_3 , chlorides, soluble aluminum) during landfilling can have a significant environmental impact [5–7], highlighting the urgent need for developing effective SAD treatment methods in the aluminum smelting sector.

SAD resource utilization processes generally both employ wet and pyrometallurgical methods. The wet process uses solutions such as sodium hydroxide, hydrochloric acid, sulfuric acid, and sodium carbonate as mediums to recover active Al_2O_3 from SAD through pressurized leaching [8–10]. However, this method generates harmful gases that pose significant environmental risks, and is associated with low efficiency and high production costs. The pyrometallurgical process involves mixing SAD with various additives and sintering at high temperatures to produce refractory insulation materials like magnesium aluminate spinel [11], refractory bricks [12], and ceramics [13, 14]. Given that SAD is primarily composed of Al_2O_3 and SiO_2 , it can sinter these materials under different experimental conditions, thus meeting industrial production requirements with reduced production costs and significant economic benefits. During calcination, the pyrometallurgical process can convert AlN into Al_2O_3 and N_2 , convert Al_4C_3 into Al_2O_3 and CO_2 , and Al into Al_2O_3 , thus reducing the reactivity of SAD. Furthermore, it can yield other high-value-added products such as ceramsite, ceramics and ceramic glass. As a method for resource regeneration of SAD, pyrometallurgical processing has gained popularity by mitigating the air pollution and safety risks associated with ammonia gas production in the wet process. To achieve higher economic gains and

minimizing environmental impacts, greater emphasis should be placed on the pyrometallurgical processing of SAD.

Ceramsite, a high-value product of high-temperature sintering, is widely used in construction, agriculture, and environmental protection [15–17] due to its excellent physical and chemical properties such as corrosion resistance, impact resistance, and low density [18, 19]. Traditionally, the primary raw materials for ceramsite are clay-based, which are processed by adding binders and pore-forming agents followed by high-temperature sintering. Currently, the solid wastes used for ceramsite production mainly include sludge [19], fly ash [20], and metal tailings [21]. The use of solid waste to produce ceramsite has become a recent hot topic. Secondary aluminum ash, rich in Al_2O_3 resources, serves as a potential precursor for ceramsite. It can be combined with municipal solid waste incineration fly ash (MSWIFA), which is rich in CaO , and municipal solid waste incineration bottom ash (MSWIBA), which is rich in SiO_2 , to form a beneficial " Al_2O_3 - SiO_2 - CaO " ternary system. After municipal solid waste (MSW) is incinerated, the reduction efficiency can exceed 80%. The incineration residue contains of 80–90% MSWIBA and 10–20% MSWIFA. Both can be collected from MSW incineration plants, which reduces costs and provides economic benefits. Some studies indicate that both SAD and MSWIFA can serve as basic raw materials for producing ceramsite that meets relevant standards. Ceramsite derived from aluminum dross exhibits a crushing efficiency of only 5.3–8.4% under a closed pressure of 35–52 MPa [22]. Additionally, high-temperature heat treatment can also remove dioxins from MSWIFA [23].

However, the specific factors influencing the compressive strength of ceramsite derived from SAD and their underlying mechanisms remain unclear. In this study, ceramsite is produced using SAD, MSWIFA, and MSWIBA as raw materials. The primary objective is to examine the effects and mechanism of various factors such as sintering temperature, raw material ball particle size, sintering time, and raw material silicon-aluminum ratio on the compressive strength of the ceramsite.

2 Materials and methods

2.1 Materials

In this study, SAD, MSWIFA, and MSWIBA are used as raw materials. All the three materials were sourced from an environmental protection technology company in Zhejiang. The SAD has a gray-black appearance and fine particle size. The MSWIFA is white and powdery, while the MSWIBA is granular with a brownish-yellow appearance.

The chemical composition of the raw materials is presented in Table 1, and their phase composition is shown in Fig. 1. The high Al_2O_3 content in SAD influences the crystallization process of ceramsite. Therefore, the addition of MWSIFA and MWSIBA, which increase the silicon content, is necessary to enhance the compressive strength of the ceramsite [24]. The flux components ($Na_2O + MgO + K_2O + CaO + Fe_2O_3$) in MWSIFA and MWSIBA constitute 55 and 36% of their

total content, respectively, thereby reducing the sintering temperature of ceramsite and energy consumption. Furthermore, AlN present in SAD generates gas during heating, making it an effective pore-forming agent. Based on preliminary experimental results and analysis of the ternary phase diagram for the mixed raw materials, the sintering temperature of the ceramsite was controlled between 1230 and 1270 °C. This range may

Table 1 Main chemical constituents of the raw materials (wt%)

Components	SiO ₂	Al ₂ O ₃	Na ₂ O	MgO	K ₂ O	CaO	Fe ₂ O ₃	Cl	S
SAD	5.95	62.4	1.74	6.89	0.34	3.05	2.49	1.57	0.72
MWSIFA	5.59	2.58	6.17	1.24	5.81	40.1	2.48	19.3	2.73
MWSIBA	34.3	8.45	4.02	2.49	2.93	20.8	6.01	1.29	0.83

MWSIFA Municipal solid waste incineration fly ash, MWSIBA Municipal solid waste incineration bottom ash

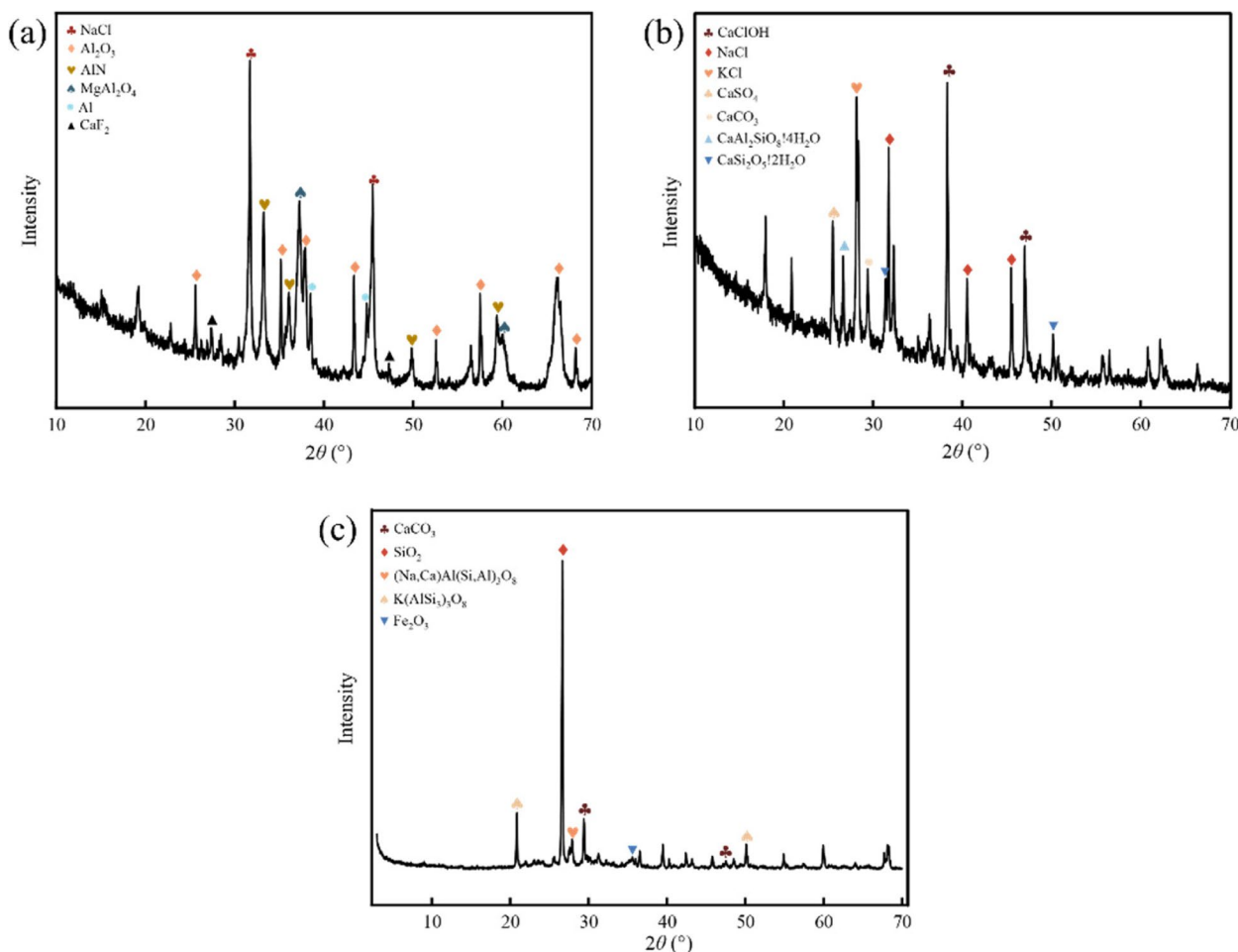


Fig. 1 XRD patterns of raw materials: **a** SAD; **b** MSWIFA; **c** MSWIBA. (MWSIFA: municipal solid waste incineration fly ash; MWSIBA: municipal solid waste incineration bottom ash)

differ from the sintering temperatures required for ceramsite derived from different raw material bases [25].

2.2 Preparation of ceramsite

First, SAD, MSWIFA, and MSWIBA were placed in an oven and dried at 105 °C for 24 h, with repeated weighing to ensure stable mass. Subsequently, the three raw materials were crushed using a grinder, and the resulting powders were sieved through a 0.15 mm mesh. The sieved materials were then stored in glass jars. The components SAD, SWIFA, and MSWIBA are weighed according to their respective ratios, with the weighed masses detailed in Table 2. A 10 mg sample of mixed raw materials with varying silicon-to-aluminum ratios was weighed and placed in separate crucibles. Each crucible was sequentially loaded into the STA 449 F3 Simultaneous Thermal Analyzer manufactured by Netzsch, Germany. Standard air was used as the ambient atmosphere. The temperature of the mixed raw materials was increased from 50 to 1400 °C at a heating rate of 10 °C min⁻¹.

Different proportions of mixed raw materials were weighed into beakers, followed by the addition of pure water at a liquid-to-solid ratio of 5:1. The mixture was then stirred thoroughly with a glass rod to ensure uniform consistency. The resulting mixture is then formed into spherical particles with diameters of 0.5, 1.0, 1.5, and 2.0 cm as required. The resulting particles are then weighed and placed in a corundum crucible (100×40×20 mm) before being transferred to a KJ-T1600-L8010WQ type 1600 degree tube furnace. One end of the tube furnace was connected to a stainless steel cylinder containing standard air, which was injected into the furnace at a flow rate of 1.5 L min⁻¹. The temperature was gradually increased at a rate of 10 °C min⁻¹ until reaching 400 °C, followed by a preheating period of 20 min. The opposite end of the tube furnace was connected to a water tank containing a dilute mixture of nitric acid and hydrogen peroxide to prevent exhaust gas from polluting the environment. Then,

Table 2 Different silicon to aluminum ratio components weighing raw material mass

Raw material silicon-aluminum ratio	SAD (g)	MSWIFA (g)	MSWIBA (g)
1	12.3	3	39
1.5	6.4	3	39
2	3.5	3	39
2.5	1.9	3	39
3	0.8	3	39

MSWIFA Municipal solid waste incineration fly ash, MSWIBA Municipal solid waste incineration bottom ash

the dried ceramsite is sintered at various temperatures determined by the experimental design (1230,1240, 1250, 1260, 1270 °C), with the heating rate maintained at 10 °C min⁻¹. Upon reaching the target temperature specified in the experimental design, the ceramsite is sintered for the duration set in the experiment (10, 20, 30, 40 min). Afterward, the ceramsite is removed from the tube furnace and allowed to cool to room temperature, thus completing the sintering process of the ceramsite product. To investigate the effects and mechanisms of various factors on the compressive strength of ceramsite, single-factor experimental schemes as shown in Table 3 are employed to conduct sintering treatments on the ceramsite. Furthermore, Table 4 presents a designed orthogonal experimental table, aimed at identifying which factors significantly affect the compressive strength of ceramsite through a limited number of experiments, in order to determine the optimal sintering conditions.

2.3 Determination of ceramsite properties

The compressive strength of the ceramsite is determined using a Universal Testing Machine. The experiment was conducted with three parallel sample groups, and the arithmetic mean of the values from these three groups was taken as the final experimental result. The compressive strength (S) is calculated using Eq. (1) [26]

$$S = \frac{2.8P_m}{\pi D^2} \tag{1}$$

where P_m denotes the load at which the ceramsite fractures, and D represents the diameter of the ceramsite.

Table 3 Single factor experimental design of ceramsite

No	Silicon-aluminum ratio	Ball particle size (cm)	Sintering temperature (°C)	Sintering time (min)
1	1	2	1260	20
2	1.5	2	1260	20
3	2	2	1260	20
4	2.5	2	1260	20
5	3	2	1260	20
6	2	0.5	1260	20
7	2	1	1260	20
8	2	1.5	1260	20
9	2	2	1230	20
10	2	2	1240	20
11	2	2	1250	20
12	2	2	1270	20
13	2	2	1260	10
14	2	2	1260	30
15	2	2	1260	40

Table 4 Orthogonal experimental design and properties of ceramsite

No	Sintering temperature (°C)	Ball particle size (cm)	Sintering time (min)	Silicon-aluminum ratio
1	1230	0.5	10	1
2	1230	1	30	2.5
3	1230	1.5	20	1.5
4	1230	2	20	3
5	1230	1	40	2
6	1240	0.5	20	2.5
7	1240	1	20	1.5
8	1240	1.5	40	3
9	1240	2	10	2
10	1240	1	30	1
11	1250	0.5	40	1.5
12	1250	1	10	3
13	1250	1.5	30	2
14	1250	2	20	1
15	1250	1	20	2.5
16	1260	0.5	30	3
17	1260	1	20	2
18	1260	1.5	20	1
19	1260	2	40	2.5
20	1260	1	10	1.5
21	1270	0.5	20	2
22	1270	1	40	1
23	1270	1.5	10	2.5
24	1270	2	30	1.5
25	1270	1	20	3

Scanning electron microscopy (SEM; HITACHI, S4800) is employed to examine the distinct morphology of the ceramsite, while X-ray diffraction (XRD; Nasdaq: BRKR, D8 ADVANCE) is utilized to investigate alterations in the ceramsite's phase composition. Additionally, Fourier-transform infrared spectroscopy (FTIR; TIANJIN GANGDONG SCI.&TECH CO., FTIR650) is applied to analyze the ceramsite's microstructure.

3 Results and discussion

3.1 Change of mechanical properties of ceramsite under the action of single factor

In this study, raw materials with significant amounts of flux components were incorporated to effectively lower the sintering temperature. As the temperature increases, the compressive strength of the ceramsite shows a pattern of initial increase, followed by a decrease, and finally an increase again within the 1260–1270 °C range. The increase in compressive strength within the 1230–1240 °C range reaches 22%. At 1250 °C, gaps form between particles, reducing the compressive strength to

its lowest point (1.09 MPa). As the sintering temperature increases to 1260 °C, numerous mineral phases melt into a liquid state and fill the gaps, making the ceramsite denser and enhancing its compressive strength. The maximum compressive strength (5.94 MPa) is ultimately achieved at 1270 °C.

As the particle size of the raw material balls increases, the compressive strength of ceramsite initially decreases and then increases. The increase in pore size and porosity within the ceramsite leads to a decrease in compressive strength, which reaches its maximum value (8.11 MPa) at a particle size of 0.5 cm. When the particle size ranges from 1.5 to 2 cm, the compressive strength increase is most pronounced at 40%.

The most substantial increase in ceramsite compressive strength occurs between 10 and 20 min of sintering time, with a less noticeable increase between 20 and 30 min. The maximum compressive strength (4.65 MPa) is reached at a sintering time of 30 min, possibly due to the ceramsite's foaming material having mostly expanded after 20 min, leading to a stable internal structure [27]. After 30 min, excessive liquid phase generation within the ceramsite makes it difficult to maintain a spherical shape.

Variations in the silicon-aluminum ratio also affect the mechanical properties of ceramsite. When silicon-aluminum ratio equals 1 and 1.5, the ceramsite cannot form effectively. This is attributed to the increasing AlN content as the SAD content increases. During sintering, substantial gas generation from intense reactions makes it difficult for ceramsite to maintain its spherical shape. Figure 2c shows that as the silicon-aluminum ratio increases from 2 to 3, the compressive strength of ceramsite continuously declines. This is due to the high SiO₂ content in the mixed raw materials and the relatively large silicon-aluminum ratio. The liquid phase in the raw material ball exhibits low viscosity, preventing a significant amount of gas from being encapsulated, which escapes by breaking through the surface melting layer, thereby affecting the foaming effect of the raw materials. The diminished expansion performance contributes to a reduction in the compressive strength of ceramsite [28]. The compressive strength of ceramsite reaches its maximum value (4.65 MPa) when silicon-aluminum ratio equals 2.

3.2 Change of mechanical properties of ceramsite under the action of multiple factors

To further refine the preparation conditions, four factors were considered: sintering temperature, raw material ball particle size, sintering duration, and silicon-aluminum ratio. The sintering temperature and silicon-aluminum ratio had five levels, while the other two factors had four levels each. The ceramsite's compressive strength

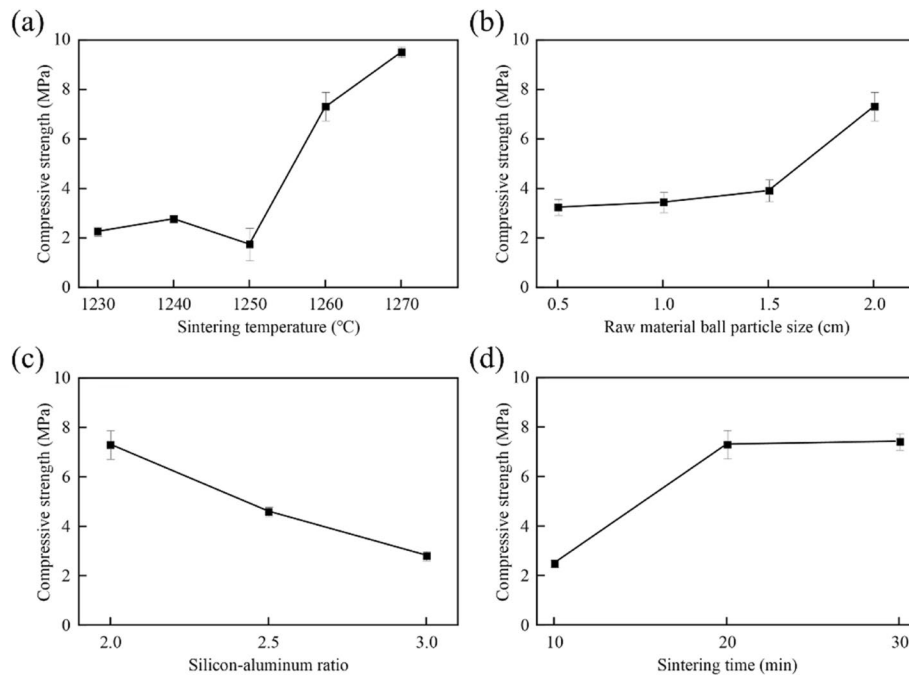


Fig. 2 The effect of single factor conditions on the compressive strength of ceramsite: **a** sintering temperature; **b** raw material ball particle size; **c** silicon-aluminum ratio; **d** sintering time

was used as the evaluation criterion. The pseudo-level method from orthogonal experimental design was used to set up the orthogonal table for this study. Initially, the L25 (5⁶) orthogonal table, the closest match, was selected, and the columns for non-existent factors 5 and 6 were removed. In the remaining table, levels that showed effective results in single-factor experiments were used to replace the factors and levels not discussed in this study. This approach allowed for the creation of an orthogonal table specific to our research needs.

The results of the orthogonal test analysis are presented in Table 5. The k-value represents the mean of the experimental outcomes for each level of a factor. A higher k-value indicates a greater influence of that level

on the experiment among all levels of the same factor. The range value (R) indicates the difference between the maximum and minimum k-values for the same factor. A larger R-value suggests that the factor is more significant and has a greater impact on performance.

As shown in Fig. 3, the particle size of raw material balls has the greatest impact on the compressive strength of ceramsite. As the particle size increases from 0.5 to 1.5 cm, the average compressive strength decreases from 13.2 to 3.54 MPa. When the particle size increases from 1.5 to 2 cm, the compressive strength increases by 16%. As shown in Table 5, a raw material ball particle size of 0.5 cm is the optimal level. The silicon-aluminum ratio of raw materials also has a significant impact on the

Table 5 Extreme difference value of each level and the average value of K

Name	Factors	Sintering temperature	Ball particle size	Sintering time	Silicon-aluminum ratio
Average value of K	1	3.52	13.20	4.80	1.35
	2	7.19	4.69	6.59	2.78
	3	4.37	3.54	7.55	7.40
	4	7.21	4.09	4.67	7.61
	5	7.92	-	-	11.05
Best Factor		5	1	3	5
R		3.93	10.65	3.18	8.68

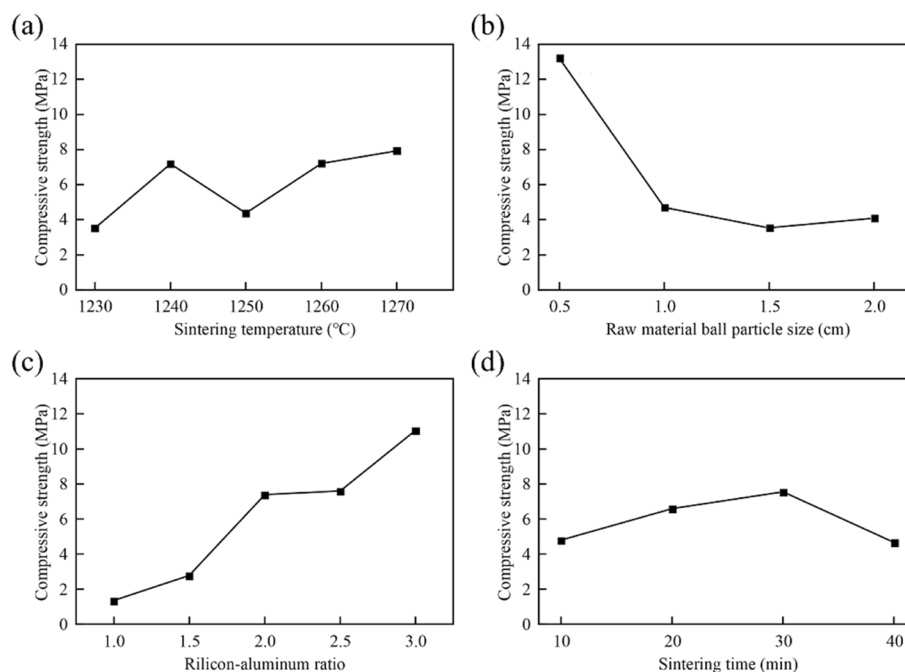


Fig. 3 The effect of multiple factors on the compressive strength of ceramsite: **a** sintering temperature; **b** raw material ball particle size; **c** silicon-aluminum ratio; **d** sintering time

compressive strength of ceramsite. The silicon-aluminum ratio is crucial in the formation of ceramics and also influences their internal crystallization processes. As the silicon-aluminum ratio increases from 1 to 3, the compressive strength increases from 1.35 to 11.05 MPa, with a silicon-aluminum ratio of 3 being the optimal level.

The effect of sintering temperature on the compressive strength of ceramsite follows this pattern: as the sintering temperature increases, the average compressive strength first increases, then decreases, and finally increases again. It reaches its lowest value (4.37 MPa) at 1250 °C and its highest value (7.92 MPa) at 1270 °C.

In contrast, time has the least effect on the compressive strength of ceramsite. As the sintering time increases, the melting process completes within the first 30 min. A longer sintering duration results in a greater liquid phase, eventually making it difficult to maintain the spherical shape and leading to a decrease in compressive strength. Based on the orthogonal test findings, to produce high-strength ceramsite, the optimal preparation conditions are a silicon-aluminum ratio of 3 for raw materials, which are kneaded into spherical particles with a diameter of 0.5 cm. The particles are then preheated in a tube furnace at 400 °C for 20 min, with a heating rate of 10 °C min⁻¹ and a standard airflow rate of 1.5 L min⁻¹. The temperature is subsequently increased to 1270 °C for 30 min of sintering, after which the ceramsite is removed and allowed to cool.

3.3 Influence mechanism of mechanical properties of ceramsite under the action of typical factors

3.3.1 Sintering temperature

The XRD patterns of ceramsite with a diameter of 2 cm and a silicon-aluminum ratio of 2, sintered at various temperatures (1230, 1240, 1250, 1260, and 1270 °C) for 20 min are shown in Fig. 4. The analysis reveals that quartz (PDF#00-046-1045-Quartz-SiO₂), albite (PDF#00-041-1480-Albite-(Na,Ca)Al(Si,Al)₃O₈), microcline (PDF#01-076-1238-Microcline-K(AlSi₃)O₈), and augite (PDF#00-041-1483-Augite-Ca(Mg,Fe,Al)(Si,Al)₂O₆) are the primary phases formed during sintering. Comparing the XRD curves at different temperature gradients, it was observed that the proportions of quartz and albite phases remained almost constant, accounting for approximately 50 and 18% of the total, respectively, at temperatures between 1230 and 1250 °C. As the temperature increased, the proportion of the albite phase rose to 20% at 1260 °C and to 23% at 1270 °C, whereas the proportion of the quartz phase decreased to 43%. This decrease in the quartz phase may be attributed to its dissolution into liquid phases formed by other components. Throughout the process, the proportions of microcline and augite phases remained relatively constant, accounting for approximately 13% of the total. The dense mineral aggregate formed by quartz, albite, and potassium feldspar phases had a robust pore skeleton structure. As the

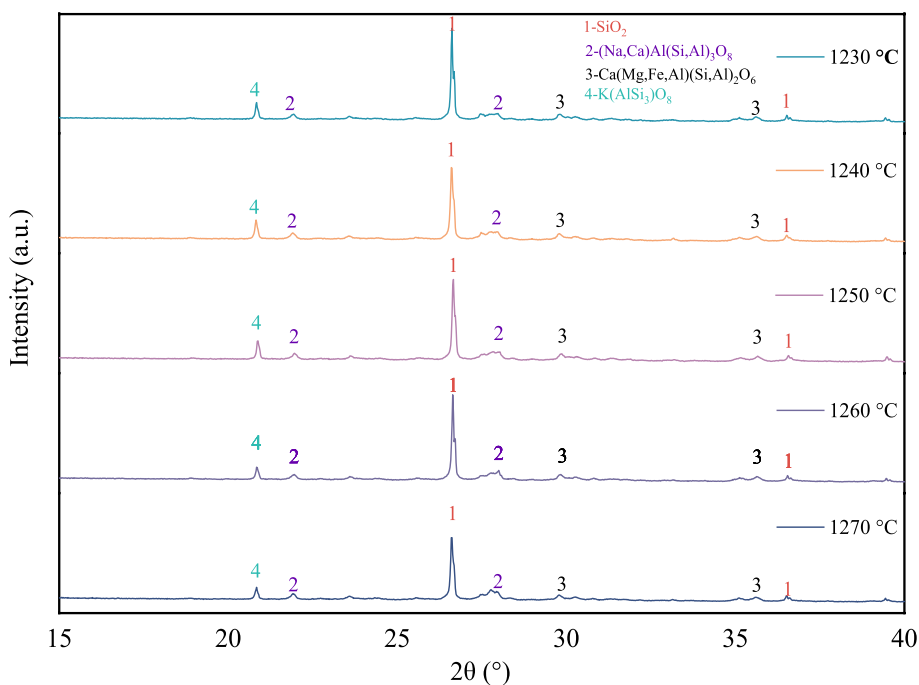


Fig. 4 XRD patterns of ceramsite at different sintering temperatures

temperature increased, the glass phase grew, enhancing the compressive strength of the ceramsite.

Figure 5 illustrates the infrared spectra of sintered ceramsite at different temperatures. With an increase in sintering temperature, the spectral bands associated with

[SiO₄] tetrahedra in the range of 800–1300 cm⁻¹ shifted towards lower wavenumber region until the temperature reached 1250 °C. However, when the temperature continued to rise to 1260 °C, the spectral bands shifted back towards higher wavenumber region. These observations

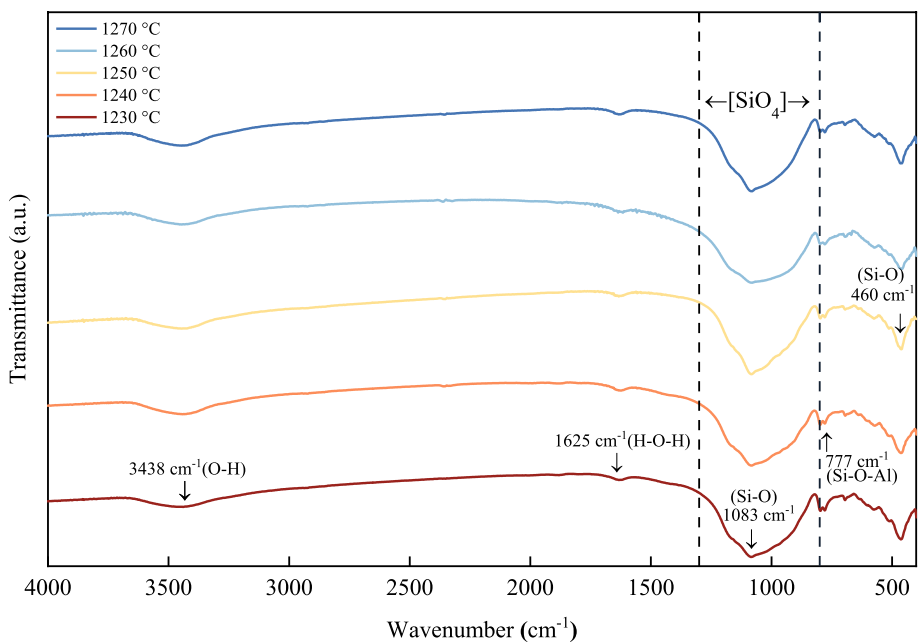


Fig. 5 Infrared spectra of ceramsite at different sintering temperatures

indicate that the degree of glass network polymerization in ceramsite decreases at 1250 °C but increases at 1260 °C. The compressive strength of ceramsite initially decreases at 1250 °C and then increases with further temperature rise.

3.3.2 Raw material ball particle size

The XRD patterns of ceramsite with particle sizes of 0.5, 1, 1.5, and 2 cm and a silicon-aluminum ratio of 2, sintered at 1260 °C for 20 min, are presented in Fig. 6. The analysis indicates that the quartz, albite, microcline, and augite phases within the ceramsite did not change significantly as the particle size of the ceramsite increased. This observation suggests that changes in the particle size of raw material balls do not affect the phase composition of ceramsite, and that compressive strength is not related to the phase. The porosity of the ceramsite was determined for all four samples, and it was observed that the porosity increased with an increase in the particle size of raw material balls. Consequently, the compressive strength of the ceramsite decreased.

Figure 7 displays the infrared spectra of sintered ceramsite with different particle sizes. The spectral bands associated with the $[\text{SiO}_4]$ tetrahedron in the range of 800 to 1300 cm^{-1} did not exhibit significant changes as the particle size increased from 0.5 to 1.0 cm. As the particle size increased from 1.0 to 1.5 cm, the spectral band shifted towards lower wavenumbers, and it became similar to the previous one. As the particle size increased from 1.5

to 2 cm, the spectral band shifted towards higher wavenumbers, indicating that the degree of glass network aggregation in ceramsite first increased in the particle size range of 0.5 to 1.5 cm, then decreased, and finally increased again at 2 cm [29]. Considering the porosity of ceramsite, as mentioned above, the compressive strength of ceramsite decreased as the particle size increased in the range of 0.5 to 1.5 cm and then increased again in the range of 1.5 to 2 cm.

3.3.3 Raw material silicon-aluminum ratio

Figure 8 shows the XRD patterns of three types of ceramsite with a particle size of 2 cm and silicon-aluminum ratio of 2, 2.5, and 3, sintered at 1260 °C for 20 min. The analysis indicates that the quartz phase increases continuously with an increase in the silicon-aluminum ratio of the raw materials. However, the albite phase in the ceramsite remains around 20% in all three silicon-aluminum ratios. In the ceramsite with a silicon-aluminum ratio of 3, the proportions of augite and microcline phases is significantly lower than the other two, indicating that excess SiO_2 cannot be converted into other crystal phases under the conditions of a sintering temperature of 1260 °C, a particle size of 2 cm for the raw material ball, and a sintering time of 20 min, suggesting that the conversion has reached saturation. The ceramsite with a silicon-aluminum ratio of 3 also exhibited a relatively loose and clear needle-like structure after sintering. As illustrated in Fig. 9, with

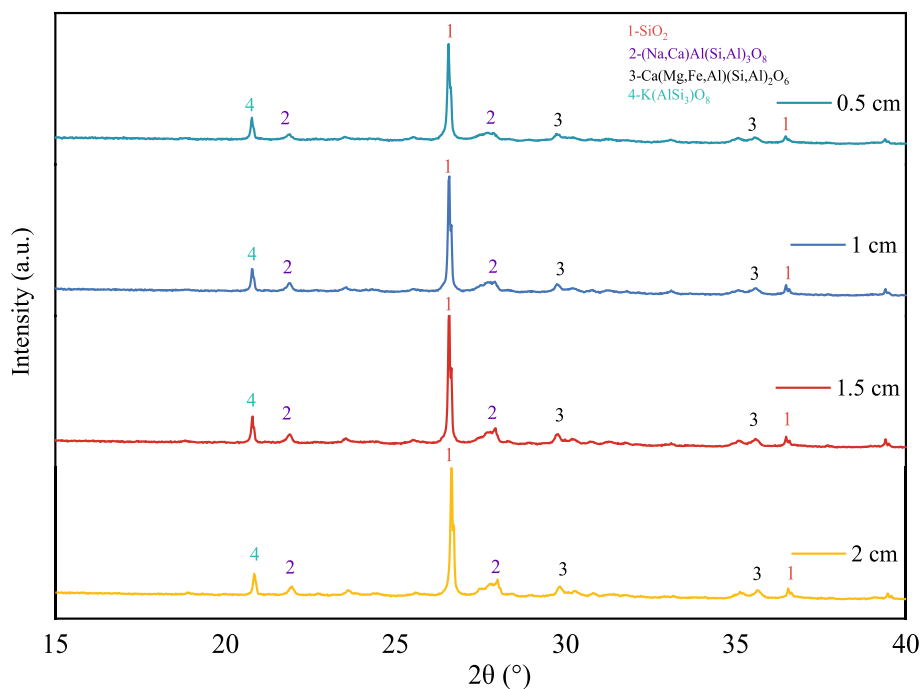


Fig. 6 XRD patterns of ceramsite with particle sizes ranging from 0.5 to 2 cm

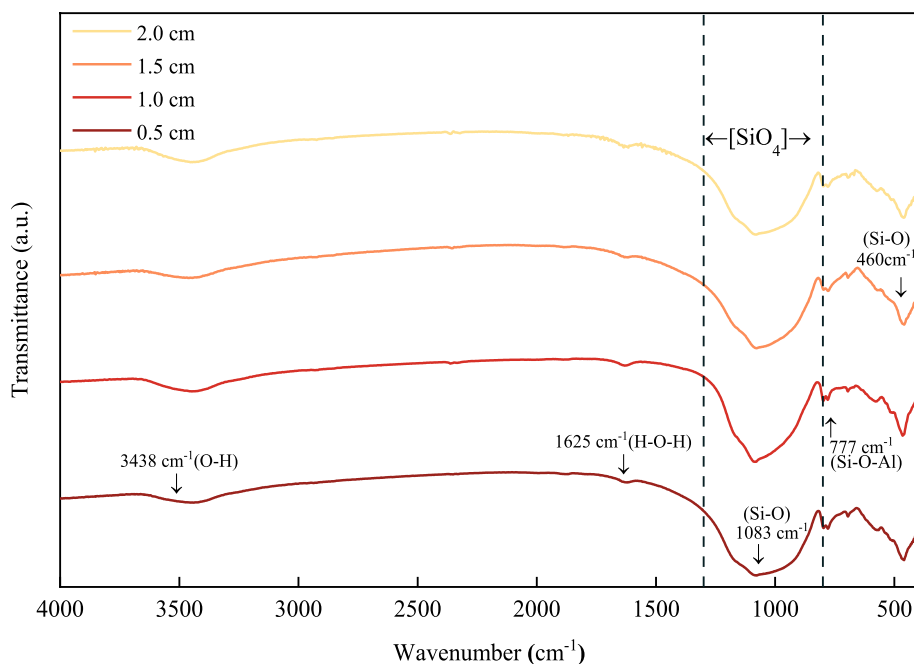


Fig. 7 Infrared spectra of ceramsite with particle sizes ranging from 0.5 to 2 cm

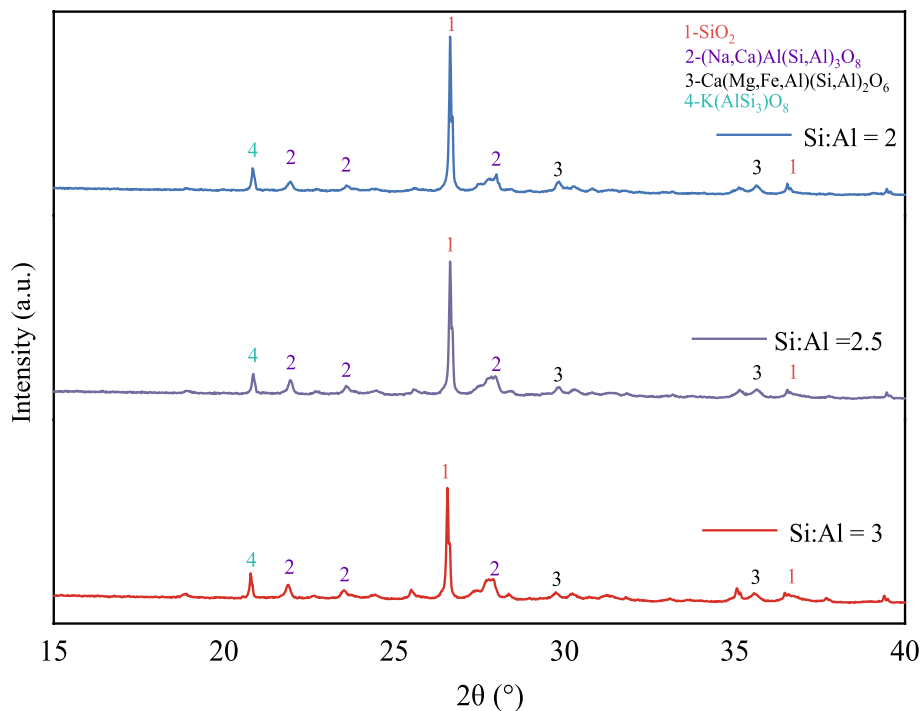


Fig. 8 XRD patterns of ceramsite under Si:Al ratios

the increase of the silicon-aluminum ratio, the ceramsite changes from smooth and dense to rough and loose, resulting in a decrease in compressive strength.

Figure 10 depicts the infrared spectra of sintered ceramsite samples with varying silicon-aluminum ratios. Within the 800 to 1300 cm^{-1} range, the bands

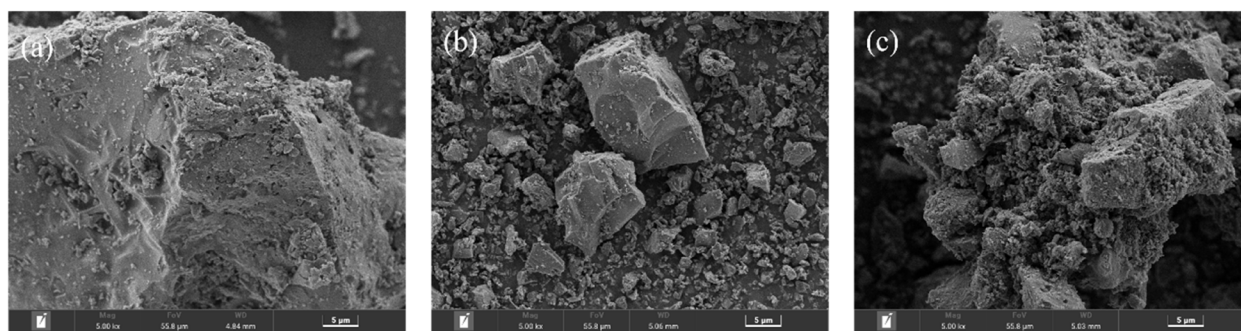


Fig. 9 SEM patterns of ceramsite under different Si:Al ratios: **a** Si:Al = 2, **b** Si:Al = 2.5, **c** Si:Al = 3

associated with $[\text{SiO}_4]$ tetrahedra display a downward shift in wavenumber when the Si:Al ratio reaches 1.5 and an upward shift when the silicon-aluminum ratio reaches 2.0. However, further changes in the silicon-aluminum ratio do not significantly affect the bands, indicating that the degree of glass network aggregation within the ceramsite initially decreases at a silicon-aluminum ratio of 1.5, then increases again at 2.0, and remains stable thereafter without significant changes [30].

3.3.4 Sintering time

Figure 11 illustrates the XRD patterns of ceramsite particles with a particle size of 2 cm and a silicon-aluminum ratio of 2 sintered at 1260 °C for 10 and 20 min.

The internal phases of the ceramsite remain mostly unchanged as the sintering time increases. Specifically, the quartz phase accounts for approximately 50%, the albite phase for approximately 20%, the microcline phase for approximately 12%, and the augite phase for about 15%. Prolonged sintering time does not facilitate the transformation into another phase.

Figure 12 presents the infrared spectra of sintered ceramsite samples with varying sintering durations. Within the 800 to 1300 cm^{-1} range, the bands associated with $[\text{SiO}_4]$ tetrahedra exhibit a continuous and slight upshift in wavenumber as the sintering duration increases. This suggests that a longer sintering duration leads to a gradual increase in glass network aggregation within the ceramsite, thereby enhancing its compressive strength.

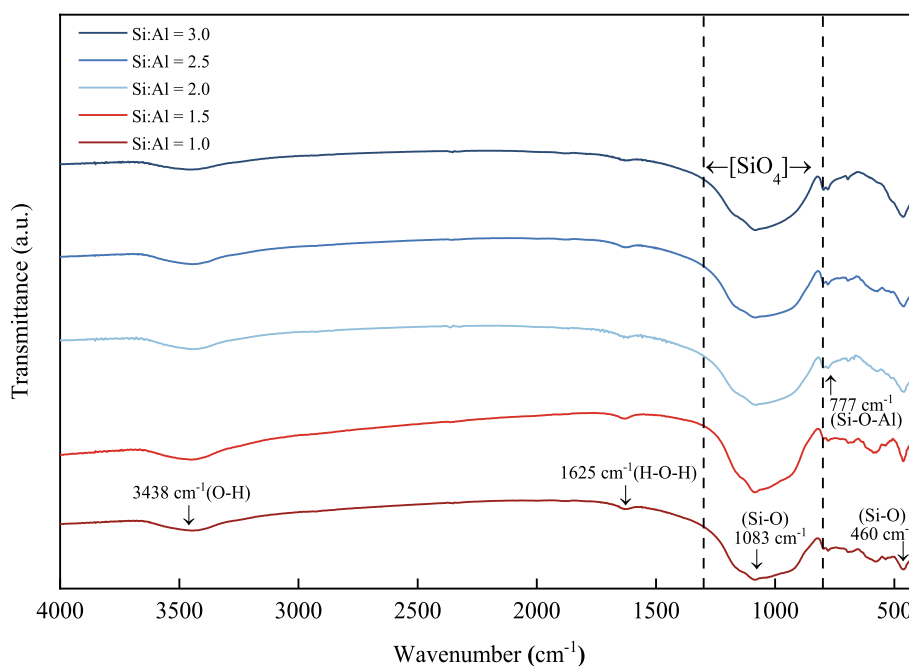


Fig. 10 Infrared spectra of ceramsite under different Si:Al ratios

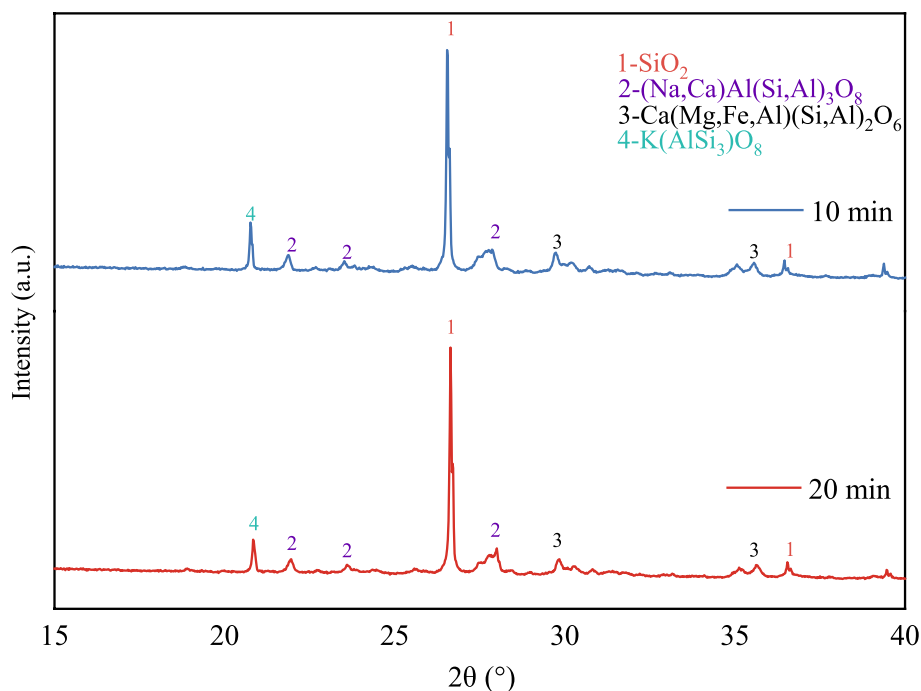


Fig. 11 XRD patterns of ceramsite sintered for 10–20 min

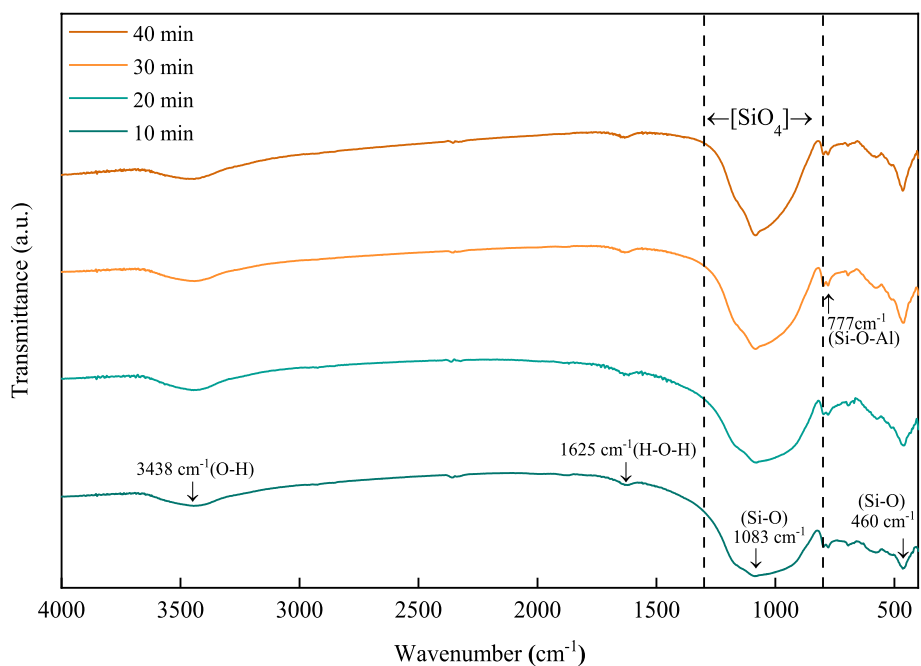


Fig. 12 Infrared spectra of ceramsite sintered for 10–40 min

3.4 Sintering mechanism analysis of creamsite

3.4.1 Thermal analysis of the individual raw material

Figure 13 presents the Thermogravimetric (TG) and Derivative TG (DTG) graphs of three different

materials heated from room temperature to 1200 °C at a heating rate of 10 °C min⁻¹. The TG curve for SAD exhibits a trend opposite to those of MSWIFA and MSWIBA. The TG curve for SAD shows distinct stages

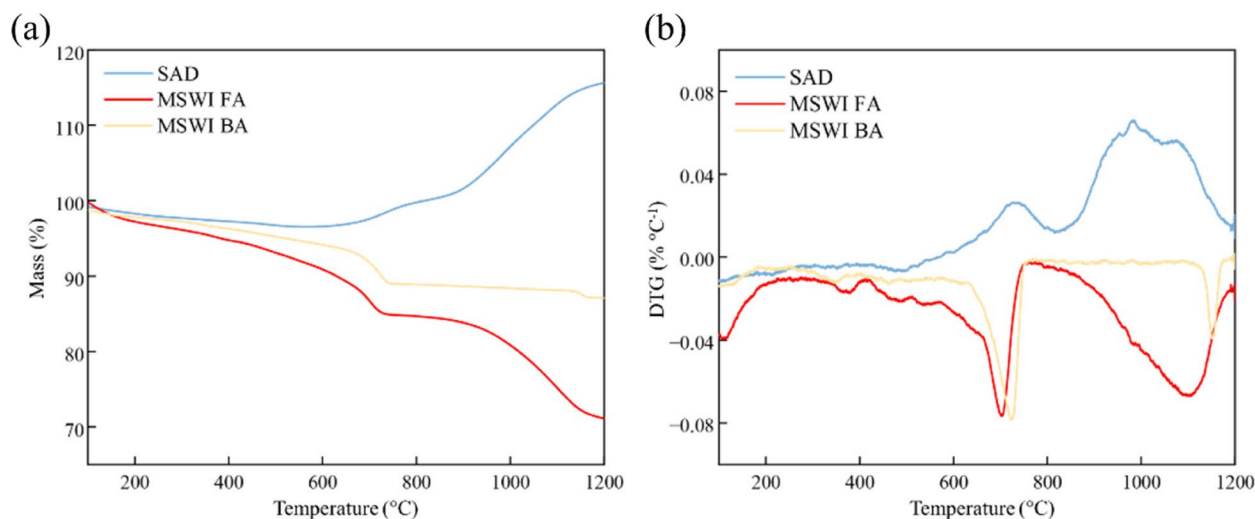


Fig. 13 a TG, (b) DTG graphs of SAD, MSWI FA, and MSWI BA. (MWSIFA: municipal solid waste incineration fly ash; MWSIBA: municipal solid waste incineration bottom ash)

of thermal reaction. The first stage, from 0 to 570 °C, is characterized by a mass loss of 3.5% due to the volatilization of moisture and gaseous products such as NH_3 , NO_x , and N_2 [31]. The second stage, spanning 570 to 1200 °C, exhibits a mass gain of approximately 19.1%. The DTG curve reveals two prominent peaks in the mass gain rate, occurring at 730 and 980 °C, indicating that Al and AlN react with O_2 to form aluminum oxide Al_2O_3 .

The TG curves of MSWIFA and MSWIBA are relatively similar, with the first stage between 50 and 400 °C primarily involving the loss of free and bound water. The second stage, from 400 to 710 °C, is characterized by the volatilization of low-boiling-point chlorides in both materials, with CaClOH in MSWIFA beginning to decompose. Between 615 and 710 °C, MSWIBA experiences a significant mass loss. The third stage, from 710 to 1200 °C, shows no significant mass loss for MSWIBA, whereas MSWIFA, which contains a high amount of chlorine, tends to produce volatile chlorides at high temperatures, and also includes the thermal decomposition of CaCO_3 . The DTG curves of both are generally similar, with MSWIBA exhibiting a minor mass loss near 1200 °C, reflected as a weight loss peak on the DTG curve, possibly due to a phase change occurring at this temperature.

3.4.2 Thermal analysis of mixed raw materials and ceramsite

Figure 14 illustrates the TG, DTG, and Differential Scanning Calorimetry (DSC) profiles of mixed raw materials

with varying silicon-aluminum ratios, heated at a rate of 10 °C min^{-1} from room temperature to 1400 °C. In general, the TG, DTG, and DSC curves of the five mixed raw materials exhibit similar trends. The TG curves generally exhibit a downward trend, the DTG curves display three distinct peaks associated with mass gain and three distinct peaks associated with mass loss, and the DSC curves indicate that the overall reactions of the mixed raw materials are exothermic.

The TG curves indicate that the initial stage of thermal reactions for the mixed raw materials occurs within the temperature range of 0–710 °C. Thermal analysis of the individual raw materials reveals that within the range of 0–400 °C, water evaporation occurs from the mixed materials. In the range of 400–710 °C, minerals such as CaClOH and CaCO_3 undergo decomposition [32]. Correspondingly, the DTG curves show a significant mass loss rate peak between 570–710 °C, suggesting that the decomposition reactions of chloride containing minerals and carbonates in fly ash and bottom ash are most intense within this temperature range.

As the temperature increases, two shoulder-like peaks appear in the DTG curves of the mixed raw materials at approximately 750 and 930 °C. These peaks correspond to the DTG curves of SAD, indicating that the slowed mass loss and partial mass gain at this stage are caused by the oxidation of Al and AlN in the secondary aluminum ash. As the temperature further increases, the mixed raw material with a silicon-aluminum ratio of 1 continues to show a trend of weight gain attributable to its higher

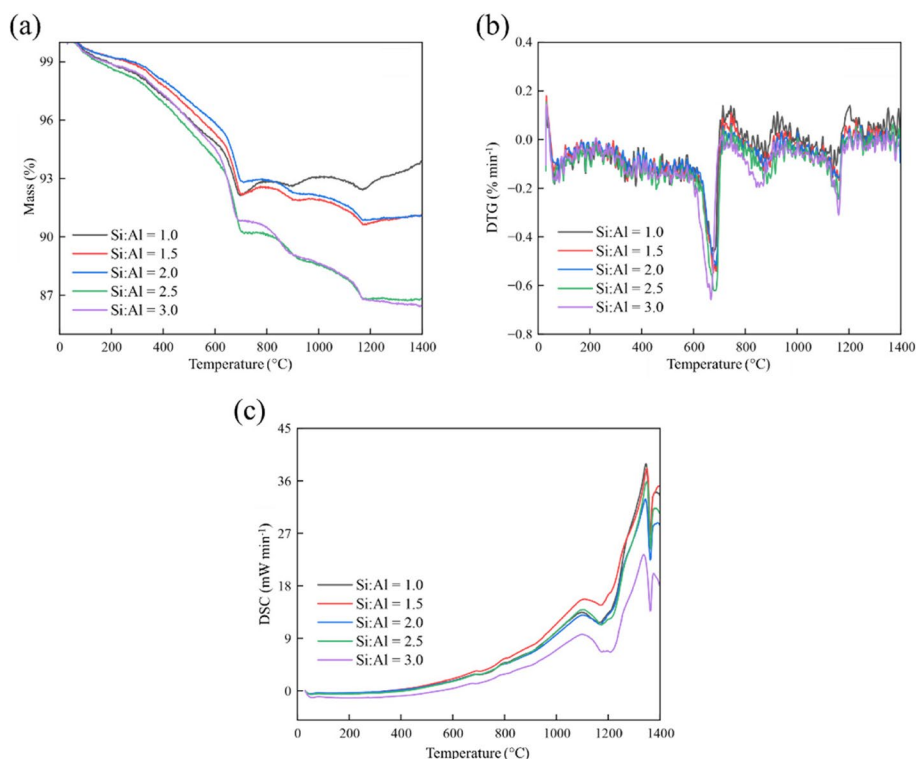


Fig. 14 Graphs of mixed raw materials: **a** TG; **b** DTG; **c** DSC

SAD content. As the silicon-aluminum ratio increases, the MSWIFA content in the mixed raw materials also increases, leading to a rise in volatile chlorides [33] and a corresponding decrease in mass. A higher silicon-aluminum ratio corresponds to greater mass loss and the faster the rate of weight loss.

At 1175 °C, an endothermic peak emerges in the DSC curve of the mixed raw materials, marking the onset of melting. This peak is prominent due to the early stage of the melting process. During this process, gases trapped within the ceramsite are released into the air, resulting in a slight decrease in mass and a corresponding peak in mass loss rate observed in the DTG curve. At approximately 1360 °C, another endothermic peak appears in the DSC curve, indicating a phase transition in the mixed raw materials.

Figure 15 combines TG and XRD analysis to predict the sintering mechanism of ceramsite with a silicon-aluminum ratio of 2, raw material ball particle size of 2 cm, and sintering time of 20 min, as it is heated from room temperature to 1270 °C. Between 0 and 400 °C, the primary process is the evaporation of water mixed in the ceramsite; from 400 to 700 °C, the primary reaction is the removal of chlorides from MSWIFA and MSWIBA at lower temperatures; between 700 and 900 °C, AlN and Al react with oxygen to form Al₂O₃, while CaCO₃ begins to decompose.

During this heating phase, gas production within the ceramsite leads to the formation of fine pores, which continues until the temperature reaches 1240 °C, at which point new mineral phases begin to form. As shown in Fig. 4, the main phases identified include feldspar phases of sodic-calcic feldspar and potassium feldspar, and a pyroxene phase of Ca(Mg,Fe,Al)(Si,Al)₂O₆, typically derived from diopside. Sodic-calcic feldspar is generally a solid solution of sodic feldspar and calcic feldspar, while potassium feldspar, being more difficult to form solid solutions with the others, exists independently. At 1250 °C, the compressive strength of the ceramsite decreases, indicating that the ceramsite has not yet reached the melting phase and remains in the crystal growth phase, where point-to-point contact between crystals increases the porosity, thereby reducing compressive strength. Subsequently, at 1260 °C, the internal structure of the ceramsite begins to melt, with the liquid phase entering the ceramsite's pores, and by 1270 °C, this trend continues.

4 Conclusions

- (1) Single-factor experiments demonstrated that the compressive strength of ceramsite initially declines and subsequently rises with increasing temperature,

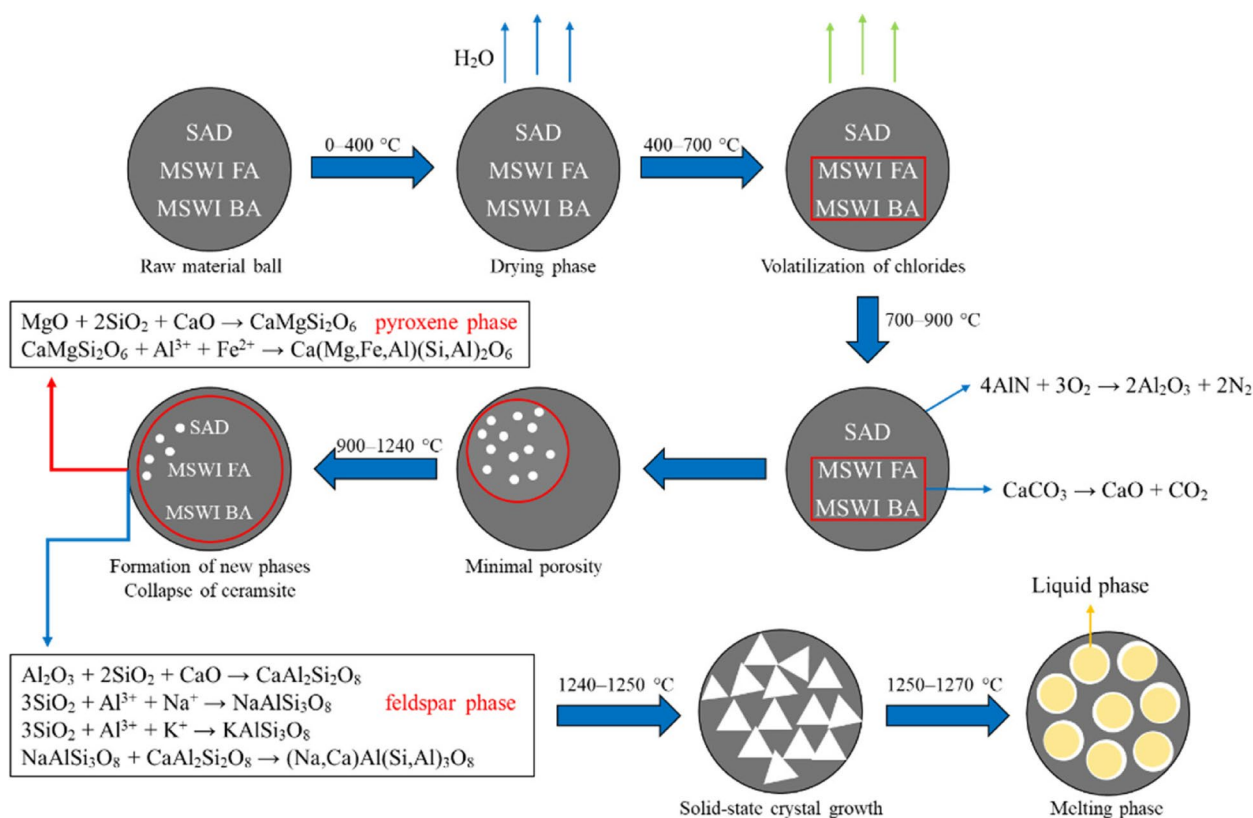


Fig. 15 Sintering mechanism of ceramsite

diminishes with larger raw material particle size, grows with longer sintering time, and reduces with a higher silicon-aluminum ratio.

- (2) Optimal conditions determined through orthogonal experiments include a raw material ratio of SAD, MSWI FA, and MSWI BA at 7.7, 6.6, and 85.7%, respectively, and a particle size of 0.5 cm. Sintering conditions involve preheating at 400 °C for 20 min, heating to 1270 °C at a rate of 10 °C min⁻¹, and sintering for 30 min.
- (3) Analysis of XRD, SEM, and FTIR spectra of the ceramsite reveals that increasing temperature promotes the transformation of the ceramsite’s quartz phase into various crystalline phases. At 1250 °C, the [SiO₄] tetrahedron band shifts to lower wavenumbers, and the degree of network polymerization decreases. At 1260 °C, the [SiO₄] tetrahedron band moves to higher wavenumbers, and the network polymerization degree increases. The ceramsite’s compressive strength declines at 1250 °C and then rises with higher temperatures. The porosity of the ceramsite grows with larger raw material particle size. In single-factor experiments, a rise in the silicon-

aluminum ratio results in SiO₂ conversion saturation, excessive loose structure, and diminished compressive strength. Prolonged sintering time enhances the ceramsite’s degree of network polymerization, thereby improving its compressive strength, likely due to more liquid phase filling the gaps and boosting network polymerization degree as time progresses.

- (4) Thermal analysis of the mixed raw materials reveals that the weight gain is attributed to the oxidation of Al and AlN in the SAD, while the weight loss is due to the decomposition and volatilization of chloride containing minerals, carbonates, and chlorides in the MSWIFA and MSWIBA.

In this study, the ceramsite underwent a melting state, which positively contributes to the stabilization of heavy metals in hazardous waste, thereby reducing environmental impact. Additionally, future research directions for alumina ash-based ceramsite include studies on its other physical properties, life cycle assessment, and economic cost evaluation. Globally, there is limited research on alumina ash-based ceramsite. By analyzing other hazardous waste-based ceramsite studies and considering

the characteristics of heavy metal pollution from SAD and chlorine pollution from MSWIFA, investigating the evolution of heavy metals and chloride during the ceramsite production process represents a crucial area for future research efforts.

Acknowledgements

The authors wish to express their gratitude for the financial and technical support provided by Qingdao University of Technology and the Chinese Research Academy of Environmental Sciences.

Authors' contributions

This study was initiated by Yufei Yang, with the experiments designed and data interpreted by Wangze He, Xinghan Zhu, and Jinzhong Yang, and experiments conducted by Wangze He. The manuscript was prepared by Wangze He, and modified by Jinzhong Yang, Qifei Huang and Yingjie Sun.

Funding

This work is partially supported by the Mineralization Mechanism of Perfluorooctane Sulfonate (PFOS) Based on Chemical Chain Reaction (CLR) (2022YSKY-33), the Technique Research & Demonstration of Co-processing Secondary Waste Dross in Typical Industrial Kiln (No. 2021ZDYF020047), the National Natural Science Foundation of China (NO. 52200179), and key technologies for environmental risk prevention and control of key solid waste risk sources in the Yellow River Basin (2022-YRUC-01-0303).

Data availability

Data will be made available on request.

Declarations

Ethics approval and consent to participate

Not applicable.

Competing interests

The authors declare no competing interests.

Author details

¹State Key Laboratory of Environmental Criteria and Risk Assessment, Chinese Research Academy of Environmental Sciences, Beijing 100012, China. ²School of Environmental and Municipal Engineering, Qingdao University of Technology, Qingdao 266520, China. ³State Environment Protection Key Laboratory of Hazardous Waste Identification and Risk Control, Chinese Research Academy of Environmental Sciences, Beijing 100012, China.

Received: 15 November 2023 Accepted: 16 December 2024

Published online: 06 January 2025

References

- Adeosun SO, Akpan EI, Dada MO. Refractory characteristics of aluminum dross-kaolin composite. *JOM*. 2014;66:2253–61.
- Shen A, Zhang J. Technologies for CO₂ emission reduction and low-carbon development in primary aluminum industry in China: A review. *Renew Sust Energ Rev*. 2024;189:113965.
- Lou B, Shen H, Liu B, Liu J, Zhang S. Recycling secondary aluminum dross to make building materials: A review. *Constr Build Mater*. 2023;409:133989.
- Srivastava A, Meshram A. A hydrometallurgical perspective of aluminium dross recycling. *Mater Today Proc*. 2023. in press.
- Gil A. Management of salt cake generated at secondary aluminum melting plants by disposal in a controlled landfill: characteristics of the controlled landfill and a study of environmental impacts. *Environ Eng Sci*. 2007;24:1234–44.
- Bruckard WJ, Woodcock JT. Recovery of valuable materials from aluminium salt cakes. *Int J Miner Process*. 2009;93:1–5.
- Abdulkadir A, Ajayi A, Hassan MI. Evaluating the chemical composition and the molar heat capacities of white aluminum dross. *Energy Procedia*. 2015;75:2099–105.
- Golaszewski J, Klemczak B, Smolana A, Golaszewska M, Cygan G, Mankel C, et al. Effect of foaming agent, binder, and density on the compressive strength and thermal conductivity of ultra-light foam concrete. *Buildings*. 2022;12:1176.
- Hu K, Reed D, Robshaw TJ, Smith RM, Ogden MD. Characterisation of aluminium black dross before and after stepwise salt-phase dissolution in non-aqueous solvents. *J Hazard Mater*. 2021;401:123351.
- Huang XL, Badawy AE, Arambewela M, Ford R, Barlaz M, Tolaymat T. Characterization of salt cake from secondary aluminum production. *J Hazard Mater*. 2014;273:192–9.
- Shi M, Li Y, Shi J. Fabrication of periclase and magnesium aluminate spinel refractory from washed residue of secondary aluminum dross. *Ceram Int*. 2022;48:7668–76.
- Zhang Y, Guo ZH, Han ZY, Xiao XY, Peng C. Feasibility of aluminum recovery and MgAl₂O₄ spinel synthesis from secondary aluminum dross. *Int J Min Met Materials*. 2019;26:309–18.
- Shen H, Liu B, Shi Z, Zhao S, Zhang J, Zhang S. Reduction for heavy metals in pickling sludge with aluminum nitride in secondary aluminum dross by pyrometallurgy, followed by glass ceramics manufacture. *J Hazard Mater*. 2021;418:126331.
- Liu J, Xu J, Zhang Y, Su Z, Xu C, Jiang T. Co-utilization of secondary aluminum dross and ferronickel slag for preparation of cordierite–mullite insulating ceramic. *J Am Ceram Soc*. 2023;106:2049–60.
- Xu GR, Zou JL, Li GB. Effect of sintering temperature on the characteristics of sludge ceramsite. *J Hazard Mater*. 2008;150:394–400.
- Wang H, Chen Z, Liu L, Ji R, Wang X. Synthesis of a foam ceramic based on ceramic tile polishing waste using SiC as foaming agent. *Ceram Int*. 2018;44:10078–86.
- Pei J, Pan X, Qi Y, Yu H, Tu G. Preparation and characterization of ultra-lightweight ceramsite using non-expanded clay and waste sawdust. *Constr Build Mater*. 2022;346:128410.
- Jing QX, Wang YY, Chai LY, Tang CJ, Huang XD, Guo H, et al. Adsorption of copper ions on porous ceramsite prepared by diatomite and tungsten residue. *T Nonferr Metal Soc*. 2018;28:1053–60.
- Tong L, Ji J, Yang J, Qian X, Li X, Wang H, et al. Sludge-based ceramsite for environmental remediation and architecture ingredients. *J Clean Prod*. 2024;448:141556.
- Xu N, Ma S, Wang N, Feng Y, Liu Y, Ren K, et al. Optimization of ternary activator for enhancing mechanical properties of carbonized cementitious material based on circulating fluidized bed fly ash. *Processes*. 2024;12:289.
- Zhong M, Meng J, Ning B, Na F, Cui T, Shi X, et al. Preparation and alkali excitation mechanism of coal gangue-iron ore tailings non-sintering ceramsite. *Constr Build Mater*. 2024;426:136209.
- Yu JL, Wen M, Jiang GB, Meng T, Wang HJ, Zhou X, et al. Effect of sintering temperature on properties of ceramic proppant prepared by mixed with secondary aluminum ash and drilling cuttings. *Chem Eng Oil Gas*. 2023;52:86–90 [In Chinese]. https://www.syytrqhg.cn/ch/reader/view_abstract.aspx?file_no=20230512&flag=1. Accessed 12 Dec 2024.
- Peng Z, Weber R, Ren Y, Wang J, Sun Y, Wang L. Characterization of PCDD/Fs and heavy metal distribution from municipal solid waste incinerator fly ash sintering process. *Waste Manage*. 2020;103:260–7.
- Shen F, Wei GS, Pang RN, Lu J, Liu FY. On lightweight ceramsite smelting from phosphorus tailings and its properties to be achieved. *J Safety Environ*. 2020;20: 2303–8. <https://doi.org/10.13637/j.jissn.1009-6094.2019.1386> [In Chinese].
- Wang H, Xu J, Liu Y, Sheng L. Preparation of ceramsite from municipal sludge and its application in water treatment: A review. *J Environ Manage*. 2021;287:112374.
- Yashima S, Kanda Y, Sano S. Relationships between particle size and fracture energy or impact velocity required to fracture as estimated from single particle crushing. *Powder Technol*. 1987;51:277–82.
- Tian X, Li A, Li S, Wang X, Qu Y, Zhao F, et al. Crystallization behavior and mechanical properties of high strength mica-containing glass-ceramics from granite wastes. *Ceram Int*. 2022;48:23119–26.
- Tsakiridis PE. Aluminium salt slag characterization and utilization – A review. *J Hazard Mater*. 2012;217–218:1–10.

29. Yang Q, Li Q, Zhang G, Shi Q, Feng H. Investigation of leaching kinetics of aluminum extraction from secondary aluminum dross with use of hydrochloric acid. *Hydrometallurgy*. 2019;187:158–67.
30. Zhu W, Wu K, Zhang S, Liu J, Yi X, Zhang L. Zero-waste progress for the synthesis of high-purity β -Sialon ceramics from secondary aluminum dross. *Adv Eng Mater*. 2021;23:2001298.
31. Wu L, Liu K, Zhou Y, Wang J, Wang H. Predicting the thermodynamics of aluminum dross denitrification of flue gas. *Calphad*. 2021;74:102315.
32. Gu Q, Wu W, Jin B. Investigation of thermal characteristics of municipal solid waste incineration fly ash under various atmospheres: A TG-FTIR study. *Thermochim Acta*. 2019;681:178402.
33. Wu X, Gu F, Su C, Wang W, Pu K, Shen D, et al. Preparing high-strength ceramsite from ferronickel slag and municipal solid waste incineration fly ash. *Ceram Int*. 2022;48:34265–72.

Publisher's Note

Springer Nature remains neutral with regard to jurisdictional claims in published maps and institutional affiliations.